Research Article | Vol. 26, No. 24 | 26 Nov 2018 | OPTICS EXPRESS 31484
Optics EXPRESS

Near-infrared chiral plasmonic metasurface absorbers

LEIXIN OUYANG,[1] WEI WANG,[1] DANIEL ROSENMANN,[2] DAVID A. CZAPLEWSKI,[2] JIE GAO,[1,3] AND XIAODONG YANG[1,4]

[1]*Department of Mechanical and Aerospace Engineering, Missouri University of Science and Technology, Rolla, MO 65409, USA*
[2]*Center for Nanoscale Materials, Argonne National Laboratory, Argonne, IL 60439, USA*
[3] *gaojie@mst.edu*
[4] *yangxia@mst.edu*

Abstract: Chirality plays an essential role in the fields of biology, medicine and physics. However, natural materials exhibit very weak chiroptical response. In this paper, near-infrared chiral plasmonic metasurface absorbers are demonstrated to selectively absorb either the left-handed or right-handed circularly polarized light for achieving large circular dichroism (CD) across the wavelength range from 1.3 μm to 1.8 μm. It is shown that the maximum chiral absorption can reach to 0.87 and that the maximum CD in absorption is around 0.70. The current chiral metasurface design is able to achieve strong chiroptical response, which also leads to high thermal CD for the local temperature increase. The high-contrast reflective chiral images are also realized with the designed metasurface absorbers. The demonstrated chiral metasurface absorbers can be applied in many areas, such as optical filters, thermal energy harvesting, optical communication, and chiral imaging.

1. Introduction

Chirality represents the asymmetry property of matter, which is important in many fields of science and engineering. Chirality has been introduced in chemistry since the 1870s [1], and the study of chirality advances our knowledge in understanding the mysteries of nature [2–11]. There are usually a pair of enantiomeric forms for optical chiral materials [12], which are two non-superimposable mirror images with different responses to the left-handed and right-handed circularly polarized (LCP and RCP) light. However, the high-efficiency chiral absorbers are not attainable from natural materials. Recently, metamaterials and metasurfaces known for exhibiting exotic electromagnetic properties [2–11] have been designed to achieve highly-efficient selective chiral absorption with various types of three-dimensional (3D) optical structures, such as double-layered L-shaped antennas [13], double-layered twisted crosses [14,15], single-layered double sectors [5], spirals [16–18], entangled structures [19,20], and letter-shaped structures [21,22]. Moreover, a deep-learning-based model has been utilized to automatically design and optimize 3D chiral metamaterials [23].

Here, we present one kind of highly-efficient chiral plasmonic metasurface absorbers working in the near-infrared wavelength region. The designed chiral metasurface absorber, consisting of a three-layer metal-dielectric-metal structure, can selectively absorb the LCP or RCP normal incident light. The results show 87% maximum chiral absorption and 70% maximum CD in absorption at the resonance wavelength across the wavelength range from 1.3 μm to 1.8 μm. The high CD in absorption is due to the special design of the top-layer metallic patterns. The resonance wavelength with the maximum CD in absorption can be easily tuned by simply changing the geometric parameters of the top-layer metallic patterns. To elucidate the mechanism of optical chiral absorption, electric field distributions and temperature distributions are mapped for the LCP and RCP incidence light. In order to further visualize the potential applications of the chiral metasurface absorbers, the high-contrast near-

#346712 https://doi.org/10.1364/OE.26.031484
Journal © 2018 Received 25 Sep 2018; revised 10 Nov 2018; accepted 12 Nov 2018; published 14 Nov 2018

Optics EXPRESS

infrared reflective chiral images of a Taichi logo depending on different incident polarizations are demonstrated. The results can be applied to many applications such as optical filters [13], thermal absorbers [24,25], optical communication devices [21], and chiral imaging and holograms [26–28].

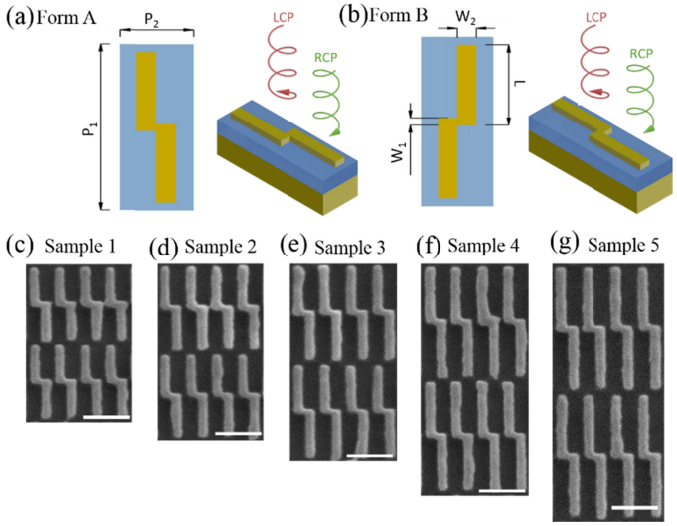

Fig. 1. (a), (b) Schematics of the chiral metasurface absorbers in Form A and Form B. (c-g) SEM images of the fabricated chiral absorbers in Form A with different geometric parameters from Sample 1 to Sample 5: P_1 = 1050, 1160, 1160, 1360 and 1460 nm; P_2 = 400, 380, 380, 380 and 380 nm; L = 450, 500, 550, 600, 650 nm; W_1 = 50 nm; W_2 = 100 nm. Scale bar represents 500 nm.

2. Design and characterization of chiral metasurface absorbers

The designed chiral metasurface absorbers are composed of a top 55 nm-thick gold (Au) layer patterned with double-rectangle resonators, a 130 nm-thick silica (SiO_2) spacer layer and a 200 nm-thick gold ground plane on a glass substrate, with thicknesses denoted as t_h, t_d and t_m, respectively. The schematics of the designed unit cells for two enantiomer forms are shown in Figs. 1(a) and 1(b). The double-rectangle pattern consists of two connected gold rectangles with overlapped space W_1, rectangle width W_2, and rectangle length L. The rectangular unit cell has the periods of P_1 and P_2. The metallic rectangle resonators are one simple type of antennas for building metasurface absorbers. By combining two rectangle resonators and shifting (or rotating) the locations of them [29], simple double-rectangle patterns with broken mirror symmetries are created in the top gold layer, allowing the designed metasurface absorber to be chiral. The multiple reflections of light inside the chiral Fabry-Pérot cavity [22] formed with the top resonator layer and the ground plane creates a chiral plasmonic resonant mode and thus enhance the selective resonant absorption of the incident circularly polarized light. The thick gold ground plane will block the transmission so that the absorption is equal to $A = 1 - R$ since $T = 0$ (where A, T and R denote the absorption, transmission and reflection, respectively). The two enantiomer forms Form A and Form B shown in Figs. 1(a) and 1(b) are mirror symmetric with each other, so that only the absorption performance of the chiral absorber in Form A is presented here. Different from other types of chiral metamaterials and metasurfaces that require complicated and precise fabrication procedures, the double-rectangle patterns of the designed chiral metasurface absorbers can be easily fabricated using focused ion beam (FIB) milling. The Au-SiO_2-Au multilayer is deposited on a glass substrate, with the Au layer deposited by sputtering and the SiO_2 layer deposited by electron-beam evaporation. Then the designed double-rectangle pattern array is milled into the top gold layer using an FIB system (FEI Helios Nanolab 600). Figures 1(c)-1(g) show the

Optics EXPRESS

scanning electron microscope (SEM) images of the top view of the fabricated chiral absorbers in Form A (from Sample 1 to Sample 5), where the geometric parameters P_1, P_2 and L of the unit cells are tuned in order to increase the resonance wavelength, while W_1 = 50 nm and W_2 = 100 nm are set as constants.

The optical reflection spectra are measured with a Fourier transform infrared spectrometer (FTIR, Nicolet 6700) connected to an infrared microscope. A set of a linear polarizer and a quarter-wave plate is used to specify the circular polarization of the incident light. Numerical simulations are also performed to investigate the optical responses of the chiral absorbers under both circular polarizations, where the permittivity of gold is taken from the experimental data with the imaginary part increased by three times and the refractive index of SiO_2 is set as a constant, with a value of 1.45. Figure 2(a) plots the measured and simulated absorption spectra of the chiral metasurface absorber in Form A (Sample 3) under LCP and RCP incidence. It is observed that the chiral plasmonic resonance is around 1.6 μm with polarization sensitive absorption, where the absorption for RCP incidence is significantly stronger than that for LCP incidence so that the CD in absorption defined as CD = $|A_{LCP} - A_{RCP}|$ is high. The slight difference between the simulated and measured absorption spectra could be caused by the defects and roughness arising from the fabrication process. The chiral resonance wavelength can be tuned by varying the geometric parameters of the top-layer double-rectangle patterns. Figure 2(b) plots the measured absorption spectra for Sample 1 to Sample 5, showing the continuous increase of the chiral resonance wavelength from 1.36 μm to 1.78 μm. The measured maximum chiral absorption can reach to 0.87 while the maximum CD in absorption is around 0.70.

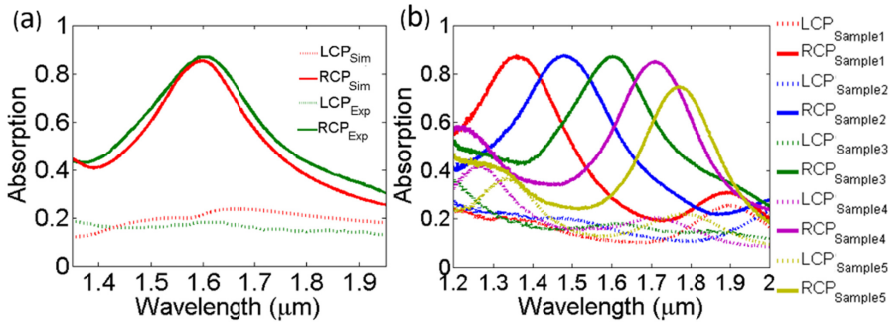

Fig. 2. (a) Simulated and measured absorption spectra of the chiral metasurface absorber in Form A (Sample 3) under LCP and RCP incidence. (b) Measured absorption spectra of the chiral metasurface absorbers in Form A from Sample 1 to Sample 5.

To reveal the mechanism responsible for the polarization sensitive absorption, electric field and temperature distributions in the chiral metasurface absorber in Form A are simulated. Figure 3(a) shows the electric field distributions across the plane 10 nm underneath the top surface of the spacer layer for both the LCP and RCP incident light at the plasmonic resonance of 1.6 μm (Sample 3). It shows that the chiral plasmonic resonance is enhanced inside the dielectric spacer layer under RCP incidence rather than LCP incidence. The simulated electric field $|\boldsymbol{E}(\boldsymbol{r})|$ and current density $\boldsymbol{J}(\mathbf{r})$ distributions at the top surface of the resonator can be seen in Fig. 3(b), and the term $\boldsymbol{J}\cdot\boldsymbol{E}$ represents the power lost to heat per unit volume. Furthermore, in order to investigate the temperature distribution in the absorber, the heat transfer equation $\nabla\cdot(-k\nabla T) = q$ is solved, where T is the temperature, k is the thermal conductivity and q is the heat generation density in metal, $q(\boldsymbol{r}) = (\omega/2)\mathrm{Im}[\varepsilon(\omega)]\varepsilon_0|\boldsymbol{E}(\boldsymbol{r})|^2$. The incident light power onto one unit cell is 10 μW, corresponding to about 30 μW/μm^2. The top and bottom boundaries are set as the fixed room temperature of 273 K and the side boundaries are periodic, which can be considered to be insulated. Heat is generated mostly inside the top-layer double-rectangle pattern, then conducted to the surrounding materials with the lower

Optics EXPRESS

temperatures, and finally reaches equilibrium. Figure 3(c) plots the simulated heat generation density distributions, *q*, at the top surface of the double-rectangle pattern at the plasmonic resonance, with the maximum value of 4.91×10^{16} W/m^3. The strong absorption of the incident RCP light can lead to high heat generation density within the top-layer metallic pattern, and thus causing a significant local temperature increase. Figure 3(d) shows the simulated temperature distributions at the top surface of the double-rectangle pattern. Due to the high thermal conductivity of gold, the top-layer double-rectangle pattern achieves a higher temperature than the surroundings, while the temperature inside the double-rectangle pattern remains almost constant, which can be seen from Figs. 3(f)-(h) with the temperature profiles along different lines marked in Fig. 3(e). The thermal circular dichroism (CD_T) is defined as $CD_T = |\Delta T_{LCP} - \Delta T_{RCP}|$ [30], where the ΔT is the local temperature increase inside the double-rectangle pattern due to the absorption of incident LCP or RCP light. Under the specific incident light power of 10 μW per unit cell, CD_T = 4 K. The relationship between CD_T, incident light power I_P and CD can be simplified as $CD_T = c_T \cdot I_P \cdot CD$, where c_T is a thermal-coefficient constant equal to 0.56 $\mu W^{-1}K^{-1}$ for each unit cell and CD = 0.70 in this case.

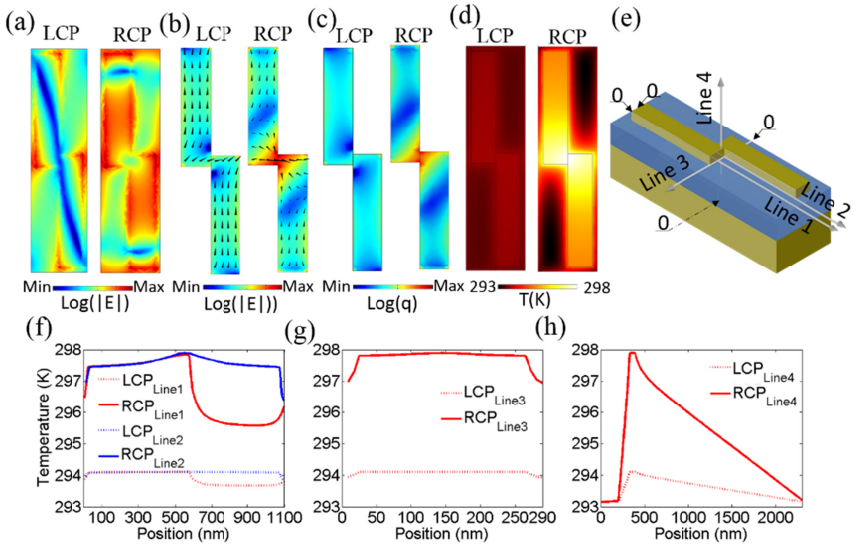

Fig. 3. (a) Simulated electric field distributions across the plane 10 nm underneath the top surface of the spacer layer under LCP and RCP incidence at 1.6 μm (Sample 3). (b) Simulated electric field and current density (arrows) distributions across the top surface of the double–rectangle pattern. (c) Simulated heat generation density distributions and (d) temperature distributions at the top surface of the double-rectangle pattern. (e) Schematics of the lines for temperature profiles. (f-h) Temperature profiles alone the lines under LCP and RCP incidence.

Next, the chiral metasurface absorbers are used to demonstrate the high-contrast near-infrared reflective images of a Taichi logo around the chiral plasmonic resonance. The incident optical beam from a laser source at 1.58 μm first passes through a combination of a linear polarizer and an achromatic quarter-wave plate to generate the circularly polarized light and then the beam is focused normally onto the Taichi Logo sample using a 20 × objective lens. The reflected light from the sample is directed and collected by an infrared camera. Figure 4(a) shows the schematic diagram of the Taichi Logo and the structure components of the fabricated sample, where chiral absorbers in both Form A and Form B are used for different areas. Figure 4(b) is a SEM image of the fabricated Taichi Logo with diameter of 45 μm. Figure 4(c) displays the reflected images of the Taichi logo under different incident polarizations from circular, elliptical to linear polarizations. Since the absorption from the chiral metasurface patterns in Form A or Form B depends on the incident polarization, the areas in Form A will appear brighter (darker) while the areas in Form B have the opposite

Optics EXPRESS

brightness under LCP (RCP) incidence. In other words, the image contrast of the Taichi Logo can be tuned by switching the incident polarization. However, when the incident light is linearly polarized, the Taichi logo can be barely observed as shown in Fig. 4(c).

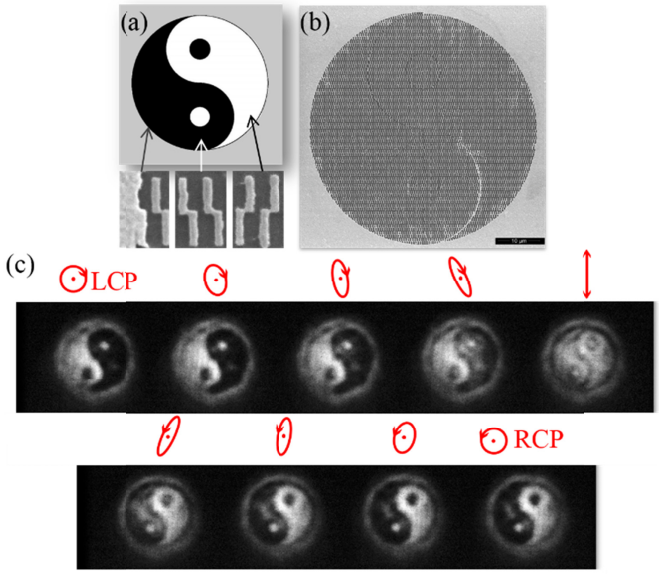

Fig. 4. (a) Schematic diagram of the Taichi Logo and the structure components of the fabricated sample with chiral metasurface patterns in Form A or Form B. (b) SEM image of the fabricated Taichi logo with diameter of 45 μm. (c) The reflected images of the Taichi logo under different incident polarizations from circular, elliptical to linear polarizations.

3. Conclusion

The near-infrared chiral plasmonic metasurface absorbers have been designed and demonstrated to perform circular polarization-dependent absorption with large circular dichroism. The strong chiroptical response of the chiral metasurface absorber also gives high thermal circular dichroism for the local temperature. The chiral plasmonic resonance of the metasurface absorber can be tuned by simply changing the geometric parameters of the unit cell. Furthermore, the high-contrast near-infrared reflective chiral images depending on different incident polarizations are also realized. These results are promising for future applications in optical filters, thermal energy harvesting, optical communication, and chiral imaging.

Funding

National Science Foundation (NSF) (DMR-1552871, ECCS-1653032); Office of Naval Research (ONR) (N00014-16-1-2408); U.S. Department of Energy, Office of Science (Contract No. DE-AC02-06CH11357).

Acknowledgment

The authors acknowledge the support from the Intelligent Systems Center and the facility support from the Materials Research Center at Missouri S&T. This work was performed, in part, at the Center for Nanoscale Materials, a U.S. Department of Energy Office of Science User Facility, and supported by the U.S. Department of Energy, Office of Science, under Contract No. DE-AC02-06CH11357.

References

1. E. L. Eliel, *Stereochemistry of Carbon Compounds* (McGraw-Hill Book Company Inc., 1962).

Optics EXPRESS

2. J. B. Pendry, "Negative refraction makes a perfect lens," Phys. Rev. Lett. **85**(18), 3966–3969 (2000).
3. N. J. Greenfield, "Using circular dichroism spectra to estimate protein secondary structure," Nat. Protoc. **1**(6), 2876–2890 (2007).
4. T. H. Chiou, S. Kleinlogel, T. Cronin, R. Caldwell, B. Loeffler, A. Siddiqi, A. Goldizen, and J. Marshall, "Circular polarization vision in a stomatopod crustacean," Curr. Biol. **18**(6), 429–434 (2008).
5. Z. Li, W. Wang, D. Rosenmann, D. A. Czaplewski, X. Yang, and J. Gao, "All-metal structural color printing based on aluminum plasmonic metasurfaces," Opt. Express **24**(18), 20472–20480 (2016).
6. L. Kang, S. P. Rodrigues, M. Taghinejad, S. Lan, K. T. Lee, Y. Liu, D. H. Werner, A. Urbas, and W. Cai, "Preserving spin states upon reflection: linear and nonlinear responses of a chiral meta-mirror," Nano Lett. **17**(11), 7102–7109 (2017).
7. L. Li, W. Wang, T. S. Luk, X. Yang, and J. Gao, "Enhanced quantum dot spontaneous emission with multilayer metamaterial nanostructures," ACS Photonics **4**(3), 501–508 (2017).
8. L. Sun, X. Yang, W. Wang, and J. Gao, "Diffraction-free optical beam propagation with near-zero phase variation in extremely anisotropic metamaterials," J. Opt. **17**(3), 035101 (2015).
9. W. Wang, D. Rosenmann, D. A. Czaplewski, X. Yang, and J. Gao, "Realizing structural color generation with aluminum plasmonic V-groove metasurfaces," Opt. Express **25**(17), 20454–20465 (2017).
10. C. D. Stanciu, F. Hansteen, A. V. Kimel, A. Kirilyuk, A. Tsukamoto, A. Itoh, and T. Rasing, "All-optical magnetic recording with circularly polarized light," Phys. Rev. Lett. **99**(4), 047601 (2007).
11. D. R. Smith, J. B. Pendry, and M. C. Wiltshire, "Metamaterials and negative refractive index," Science **305**(5685), 788–792 (2004).
12. E. Plum and N. I. Zheludev, "Chiral mirrors," Appl. Phys. Lett. **106**(22), 221901 (2015).
13. M. H. Li, L. Y. Guo, J. F. Dong, and H. L. Yang, "An ultra-thin chiral metamaterial absorber with high selectivity for LCP and RCP waves," J. Phys. D **47**(18), 185102 (2014).
14. C. Huang, X. L. Ma, M. B. Pu, G. W. Yi, Y. Q. Wang, and X. G. Luo, "Dual-band 90° polarization rotator using twisted split ring resonators array," Opt. Commun. **291**, 345–348 (2013).
15. S. Zhang, H. Wei, K. Bao, U. Håkanson, N. J. Halas, P. Nordlander, and H. Xu, "Chiral surface plasmon polaritons on metallic nanowires," Phys. Rev. Lett. **107**(9), 096801 (2011).
16. M. Esposito, V. Tasco, M. Cuscunà, F. Todisco, A. Benedetti, I. Tarantini, M. D. Giorgi, D. Sanvitto, and A. Passaseo, "Nanoscale 3D chiral plasmonic helices with circular dichroism at visible frequencies," ACS Photonics **2**(1), 105–114 (2015).
17. M. Esposito, V. Tasco, F. Todisco, A. Benedetti, D. Sanvitto, and A. Passaseo, "Three dimensional chiral metamaterial nanospirals in the visible range by vertically compensated focused ion beam induced-deposition," Adv. Opt. Mater. **2**(2), 154–161 (2014).
18. J. K. Gansel, M. Thiel, M. S. Rill, M. Decker, K. Bade, V. Saile, G. von Freymann, S. Linden, and M. Wegener, "Gold helix photonic metamaterial as broadband circular polarizer," Science **325**(5947), 1513–1515 (2009).
19. E. Togan, Y. Chu, A. S. Trifonov, L. Jiang, J. Maze, L. Childress, M. V. G. Dutt, A. S. Sørensen, P. R. Hemmer, A. S. Zibrov, and M. D. Lukin, "Quantum entanglement between an optical photon and a solid-state spin qubit," Nature **466**(7307), 730–734 (2010).
20. H. S. Park, T. T. Kim, H. D. Kim, K. Kim, and B. Min, "Nondispersive optical activity of meshed helical metamaterials," Nat. Commun. **5**(1), 5435 (2014).
21. W. Li, Z. J. Coppens, L. V. Besteiro, W. Wang, A. O. Govorov, and J. Valentine, "Circularly polarized light detection with hot electrons in chiral plasmonic metamaterials," Nat. Commun. **6**(1), 8379 (2015).
22. B. Tang, Z. Y. Li, E. Palacios, Z. H. Liu, S. Butun, and K. Aydin, "Chiral-selective plasmonic metasurface absorbers operating at visible frequencies," IEEE Photonics Technol. Lett. **29**(3), 295–298 (2017).
23. W. Ma, F. Cheng, and Y. Liu, "Deep-learning-enabled on-demand design of chiral metamaterials," ACS Nano **12**(6), 6326–6334 (2018).
24. H. X. Deng, T. C. Wang, J. Gao, and X. D. Yang, "Metamaterial thermal emitters based on nanowire cavities for high-efficiency thermophotovoltaics," J. Opt. **16**(3), 035102 (2014).
25. X. Liu, T. Tyler, T. Starr, A. F. Starr, N. M. Jokerst, and W. J. Padilla, "Taming the blackbody with infrared metamaterials as selective thermal emitters," Phys. Rev. Lett. **107**(4), 045901 (2011).
26. Y. Chen, J. Gao, and X. Yang, "Chiral metamaterials of plasmonic slanted nanoapertures with symmetry breaking," Nano Lett. **18**(1), 520–527 (2018).
27. Q. Wang, E. Plum, Q. L. Yang, X. Q. Zhang, Q. Xu, Y. H. Xu, J. G. Han, and W. L. Zhang, "Reflective chiral meta-holography: multiplexing holograms for circularly polarized waves," Light Sci. Appl. **7**(1), 25 (2018).
28. Y. Chen, X. Yang, and J. Gao, "Spin-controlled wavefront shaping with plasmonic chiral geometric metasurfaces," Light Sci. Appl. **7**(1), 84 (2018).
29. Z. Wang, H. Jia, K. Yao, W. Cai, H. Chen, and Y. Liu, "Circular dichroism metamirrors with near-perfect extinction," ACS Photonics **3**(11), 2096–2101 (2016).
30. X. T. Kong, L. Khosravi Khorashad, Z. Wang, and A. O. Govorov, "Photothermal circular dichroism induced by plasmon resonances in chiral metamaterial absorbers and bolometers," Nano Lett. **18**(3), 7b05446 (2018).